

# Geometric Mechanics of Periodic Pleated Origami

Z. Y. Wei,<sup>1</sup> Z. V. Guo,<sup>1</sup> L. Dudte,<sup>1</sup> H. Y. Liang,<sup>1</sup> and L. Mahadevan<sup>1,2,\*</sup>

<sup>1</sup>*School of Engineering and Applied Sciences, Harvard University, Cambridge, Massachusetts 02138, USA*

<sup>2</sup>*Department of Physics, Harvard University, Cambridge, Massachusetts 02138, USA*

(Received 25 November 2012; revised manuscript received 16 February 2013; published 21 May 2013)

Origami structures are mechanical metamaterials with properties that arise almost exclusively from the geometry of the constituent folds and the constraint of piecewise isometric deformations. Here we characterize the geometry and planar and nonplanar effective elastic response of a simple periodically folded Miura-ori structure, which is composed of identical unit cells of mountain and valley folds with four-coordinated ridges, defined completely by two angles and two lengths. We show that the in-plane and out-of-plane Poisson's ratios are equal in magnitude, but opposite in sign, independent of material properties. Furthermore, we show that effective bending stiffness of the unit cell is singular, allowing us to characterize the two-dimensional deformation of a plate in terms of a one-dimensional theory. Finally, we solve the inverse design problem of determining the geometric parameters for the optimal geometric and mechanical response of these extreme structures.

DOI: [10.1103/PhysRevLett.110.215501](https://doi.org/10.1103/PhysRevLett.110.215501)

PACS numbers: 81.05.Xj, 46.70.De

Metamaterials are defined as materials whose structure and constitution allows them to have unusual emergent properties, such as negative refractive index optical metamaterials [1], or negative Poisson ratio mechanical metamaterials [2]. Here, we focus on origami-inspired mechanical metamaterials that arise as folded and pleated structures in a variety of natural systems including insect wings [3], leaves [4], and flower petals [5]. Using the presence of creases in these systems allows one to fold and unfold an entire structure simultaneously and design deployable structures such as solar sails [6] and foldable maps [7], and auxetic structural materials such as foams [8], and microporous polymers [9]. Indeed, folded sheets with reentrant geometries serve as models for crystal structures [10,11], molecular networks [12], and glasses [2] in a variety of physical applications. Complementing these studies, there has been a surge of interest in the mathematical properties of these folded structures [13–15], and some recent qualitative studies on the engineering aspects of origami [16–18]. In addition, the ability to create them *de novo* without a folding template, as a self-organized buckling pattern when a stiff skin resting on a soft foundation is subject to biaxial compression [19–21] has opened up a range of questions associated with their assembly in space and time, and their properties. However, most past quantitative work on these materials has been limited to understanding their behavior in two dimensions, either by considering their auxetic behavior in the plane, or the bending of a one-dimensional corrugated strip. In this Letter, we characterize the three-dimensional elastic response, Poisson's ratios, and rigidities of perhaps the simplest such mechanical metamaterial based on origami—a three-dimensional periodically pleated or folded structure, the Miura-ori pattern, [Fig. 1(a)] which is defined completely in terms of two angles and two lengths.

The geometry of the unit cell embodies the basic element in all nontrivial pleated structures—the mountain or valley fold, wherein four edges (folds) come together at a single vertex, as shown in Fig. 1(d). It is parametrized by two dihedral angles  $\theta \in [0, \pi]$ ,  $\beta \in [0, \pi]$ , and one oblique angle  $\alpha$ , in a cell of length  $l$ , width  $w$ , and height  $h$ . We treat the structure as being made of identical periodic rigid skew plaquettes joined by elastic hinges at the ridges. The structure can deploy uniformly in the plane [Fig. 1(b)] by having each constituent skew plaquette in a unit cell

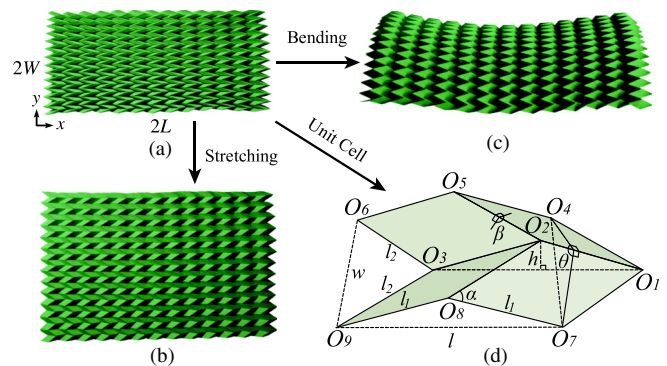


FIG. 1 (color online). Geometry of Miura-ori pattern. (a) A Miura-ori plate folded from a letter size paper contains 13 by 13 unit cells (along  $x$  and  $y$  directions, respectively), with  $\alpha = 45^\circ$  and  $l_1 = l_2 = l_e$ . The plate dimension is  $2L$  by  $2W$ . (b) In-plane stretching behavior of a Miura-ori plate when pulled along the  $x$  direction shows it expands in all directions; i.e., it has a negative Poisson's ratio. (c) Out-of-plane bending behavior of a Miura-ori plate when a symmetric bending moment is applied on boundaries  $x = \pm L$  shows a saddle shape, consistent with that, in this mode of deformation, its Poisson's ratio is positive. (d) Unit cell of Miura-ori is characterized by two angles  $\alpha$  and  $\theta$  given  $l_1$  and  $l_2$  and is symmetric about the central plane passing through  $O_1 O_2 O_3$ .

rotate rigidly about the connecting elastic ridges. Then the ridge lengths  $l_1$ ,  $l_2$ , and  $\alpha \in [0, \pi/2]$  are constant through folding or unfolding, so that we may choose  $\theta$  (or equivalently  $\beta$ ) to be the only degree of freedom that completely characterizes a Miura-ori cell. The geometry of the unit cell implies that

$$\beta = 2\sin^{-1}[\zeta \sin(\theta/2)], \quad l = 2l_1\zeta, \quad (1)$$

$$w = 2l_2\xi \quad \text{and} \quad h = l_1\zeta \tan\alpha \cos(\theta/2),$$

where the dimensionless width and height are

$$\xi = \sin\alpha \sin(\theta/2) \quad \text{and} \quad \zeta = \cos\alpha(1 - \xi^2)^{-1/2}. \quad (2)$$

We see that  $\beta$ ,  $l$ ,  $w$ , and  $h$  change monotonically as  $\theta \in [0, \pi]$ , with  $\beta \in [0, \pi]$ ,  $l \in 2l_1[\cos\alpha, 1]$ ,  $w \in 2l_2[0, \sin\alpha]$ , and  $h \in l_1[\sin\alpha, 0]$ . As  $\alpha \in [0, \pi/2]$ , we see that  $\beta \in [\theta, 0]$ ,  $l \in [2l_1, 0]$ ,  $w \in [0, 2l_2 \sin(\theta/2)]$ , and  $h \in [0, l_1]$ . The geometry of the unit cell implies a number of interesting properties associated with the expansion kinematics of a folded Miura-ori sheet, including design optimization for packing, and the study of nearly orthogonal folds when  $\alpha \approx \pi/2$ , the singular case corresponding to the common map fold where the folds are all independent (SI-1 in Supplemental Material [22]). To minimize algebraic complexity and focus on the main consequences of isometric deformations of these structures, we will henceforth assume each plaquette is a rhombus, i.e.,  $l_1 = l_2 = l_e$ .

The planar response of Miura-ori may be characterized in terms of two quantities—the Poisson's ratio which describes the coupling of deformations in orthogonal directions, and the stretching rigidity which characterizes its planar mechanical stiffness. The linearized planar Poisson's ratio is defined as

$$\nu_{wl} \equiv -\frac{dw/w}{dl/l} = 1 - \xi^{-2}. \quad (3)$$

It immediately follows that the reciprocal Poisson's ratio  $\nu_{lw} = 1/\nu_{wl}$ . Because  $\xi \leq 1$ , the in-plane Poisson's ratio  $\nu_{wl} < 0$  [Fig. 2(a)]; i.e., Miura-ori is an auxetic material. The limits on  $\nu_{wl}$  may be determined by considering the extreme values of  $\alpha$ ,  $\theta$ , since  $\nu_{wl}$  monotonically increases in both variables. Using the expression (2) in (3) and expanding the result shows that  $\nu_{wl}|_{\alpha \rightarrow 0} \sim \alpha^{-2}$ , and thus,  $\nu_{wl}|_{\theta} \in (-\infty, -\cot^2(\theta/2)]$ , while  $\nu_{wl}|_{\theta \rightarrow 0} \sim \theta^{-2}$  and, thus,  $\nu_{wl}|_{\alpha} \in (-\infty, -\cot^2\alpha]$ . When  $(\alpha, \theta) = (\pi/2, \pi)$ ,  $\nu_{wl} = 0$  so that the two orthogonal planar directions may be folded or unfolded independently, as in traditional map folding. Indeed, this is the unique state for which nonparallel folds are independent, and it might surprise the reader that, with few exceptions, this is the way maps are folded—makes unfolding easy, but folding frustrating! The Poisson's ratios related to height changes,  $\nu_{hl}$  and  $\nu_{wh}$  can also be determined using similar arguments (SI-2.1 in Supplemental Material [22]).

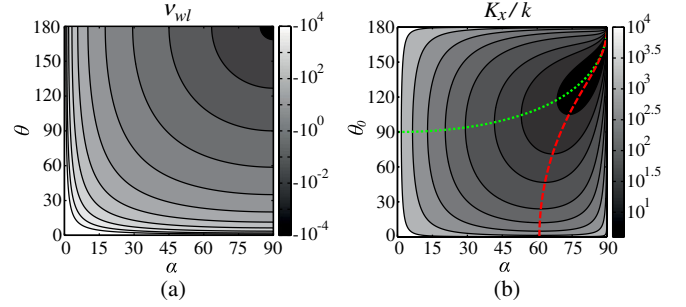


FIG. 2 (color online). In-plane stretching response of a unit cell. (a) Contour plot of Poisson's ratio  $\nu_{wl}$ .  $\nu_{wl}$  shows that it monotonically increases with both  $\alpha$  and  $\theta$ .  $\nu_{wl}|_{\alpha} \in [-\infty, -\cot^2\alpha]$ , and  $\nu_{wl}|_{\theta} \in [-\infty, -\cot^2(\theta/2)]$ . (b) Contour plot of the dimensionless stretching rigidity  $K_x/k$ . The green dotted curve indicates the optimal design angle pairs that correspond to the minima of  $K_x|_{\alpha}$ . The red dashed curve indicates the optimal design angle pairs that correspond to the minima of  $K_x|_{\theta}$ . See the text for details.

To calculate the in-plane stiffness of the unit cell, we note that the potential energy of a unit cell deformed by a uniaxial force  $f_x$  in the  $x$  direction is  $H = U - \int_{\theta_0}^{\theta} f_x (dl/d\theta') d\theta'$ , assuming that the elastic energy of a unit cell is stored only in the elastic hinges which allow the rigid plaquettes to rotate isometrically, with  $U = kl_e(\theta - \theta_0)^2 + kl_e(\beta - \beta_0)^2$ ,  $k$  being the hinge spring constant,  $\theta_0$  and  $\beta_0 [= \beta(\alpha, \theta_0)]$  being the natural dihedral angles in the undeformed state. Then, the external force  $f_x$  at equilibrium is determined by the relation  $\delta H/\delta\theta = 0$ , while the stretching rigidity in the  $x$  direction is given by

$$K_x(\alpha, \theta_0) \equiv \left. \frac{df_x}{d\theta} \right|_{\theta_0} = \frac{4k[(1 - \xi_0^2)^2 + \cos^2\alpha]}{(1 - \xi_0^2)^{1/2} \cos\alpha \sin^2\alpha \sin\theta_0}, \quad (4)$$

where  $\xi_0 = \xi(\alpha, \theta_0)$  and  $\xi$  is defined in (2). To understand the bounds on  $K_x$ , we expand (4) in the vicinity of the extreme values of  $\alpha$  and  $\theta_0$  which gives us  $K_x|_{\alpha \rightarrow 0} \sim \alpha^{-2}$ ,  $K_x|_{\alpha \rightarrow \pi/2} \sim (\pi/2 - \alpha)^{-1}$ ,  $K_x|_{\theta_0 \rightarrow 0} \sim \theta_0^{-1}$ , and  $K_x|_{\theta_0 \rightarrow \pi} \sim (\pi - \theta_0)^{-1}$ . As expected, we see that  $K_x$  has a singularity at  $(\alpha, \theta_0) = (\pi/2, \pi)$ , corresponding to the case of an almost flat, unfolded orthogonal Miura sheet.

We note that  $K_x$  is not a monotonic function of the geometric variables defining the unit cell,  $\alpha$  and  $\theta_0$ . Setting  $\partial_{\theta_0} K_x|_{\alpha} = 0$  and  $\partial_{\alpha} K_x|_{\theta_0} = 0$  allows us to determine the optimal design curves,  $\theta_{0m}(\alpha)$  [green dotted curve in Fig. 2(b)] and  $\alpha_m(\theta_0)$  [red dashed curve in Fig. 2(b)] that yield the minimum value of the stiffness  $K_x$  as a function of these parameters. Along these curves, the stiffness varies monotonically. Analogous arguments allow us to determine the orthogonal stretching rigidity  $K_y$ , which is related geometrically to  $K_x$  via the design angles  $\alpha$  and  $\theta$  (SI-2.2, 2.3 in Supplemental Material [22]). Since piecewise isometric deformations only allow for planar folding as the only possible motion using rigid

rhombus plaquettes in Miura-ori plates (SI-3.1 in Supplemental Material [22]), the in-plane shear elastic constant is infinite, an unusual result given that most normal materials may be sheared easily and yet strongly resist volumetric changes.

To understand the nonplanar bending response of Miura-ori, we must consider the conditions when it is possible to bend a unit cell isometrically, i.e., with only rotations of the plaquettes about their linking hinges. Minimally, isometric deformations require the introduction of one additional diagonal fold into each plaquette [Fig. 3(a)], either a short one (e.g.,  $O_2O_7$ ) or a long one (e.g.,  $O_1O_8$ ). Here, we adopt the short fold, as a result of which four additional degrees of freedom arise in each unit cell and allow for both symmetric bending and asymmetric twisting, depending on whether the rotations are symmetric or not. The out-of-plane bending Poisson's ratio  $\nu_b \equiv -\kappa_y/\kappa_x$  [23], where  $\kappa_x, \kappa_y$  are the effective curvatures of the Miura-ori sheet in the  $x$  and  $y$  directions given by

$$\begin{aligned}\kappa_x &= \frac{\cos(\alpha/2) \sin(\theta/2)}{2l_e \sqrt{1-\xi^2}} (\phi_2 + \phi_4), \\ \kappa_y &= -\frac{\sqrt{1-\xi^2}}{4l_e \sin(\alpha/2) \xi} (\phi_2 + \phi_4),\end{aligned}\quad (5)$$

with  $\kappa_x$  being the dihedral angle between plane  $O_6O_3O_9$  and  $O_4O_1O_7$  [Fig. 3(a)] projected onto the  $x$  direction over the unit cell length (SI-3.2 in Supplemental Material [22]), and  $\kappa_y$  being the dihedral angle between plane  $O_4O_5O_6$  and  $O_7O_8O_9$  projected onto the  $y$  direction over the unit cell width. The angles  $\phi_2, \phi_4$  characterize rotations about internal folds  $\vec{O_7O_2}$  and  $\vec{O_8O_3}$ , respectively, and are deemed positive according to the right-hand rule. We note that although there are a total of five deformation angles [Fig. 3(a)], both  $\kappa_x$  and  $\kappa_y$  depend only on  $\phi_2$  and  $\phi_4$ . This is because of the symmetry of deformations about the  $xoz$  plane;  $\phi_3$  and  $\phi_5$  are functions of  $\phi_1$  and  $\phi_2$  (Eq. S.28 in Supplemental Material [22]), and the case that  $\phi_1$  changes, while keeping  $\phi_2$  and  $\phi_4$  zero, corresponds to the planar stretch of a unit cell, so  $\phi_1$  does not contribute to both curvatures. This is consistent with our intuition that bending a unit cell requires the bending of plaquettes. The Poisson's ratio for bending, thus, is

$$\nu_b = -\frac{\kappa_y}{\kappa_x} = -1 + \xi^{-2} = -\nu_{wl}, \quad (6)$$

where the last equality follows from Eqs. (3) and (5). If the original plaquettes are allowed to fold along the long diagonals instead [e.g.,  $O_8O_1$  in Fig. 3(a)], the new curvature components  $\kappa_x$  and  $\kappa_y$  are still given by (5) with  $\alpha$  being replaced by  $\pi - \alpha$  (SI-3.3 in Supplemental Material [22]), and  $\phi_2, \phi_4$  now being rotations about axis  $\vec{O_8O_1}$  and  $\vec{O_9O_2}$ , respectively. Therefore,  $\nu_b = -\kappa_y/\kappa_x = -\nu_{wl}$ . We note that in nonplanar bending, the sheet behaves like a normal material, deforming into a saddle as shown in Fig. 1(c). The surprising result, that the in-plane Poisson's ratio is equal in magnitude but opposite in sign to the out-of-plane Poisson ratio, is independent of the mechanical properties of the sheet and is a consequence of geometry alone. Although our analysis is limited to the case when the deformation involves only small changes in the angles about their natural values, this is not as restrictive as it seems, since small changes to the unit cell can still lead to very large global deformations of the entire sheet.

Given our understanding of the geometry of bending in a unit cell, we now derive an effective continuum elastic theory for a Miura-ori plate that consists of many unit cells. Our calculations for the unit cell embodied in (5) show that  $\kappa_x/\kappa_y$  is only a function of the design angles  $\alpha$  and  $\theta$ , and independent of deformation angles; i.e., one cannot independently control  $\kappa_x$  and  $\kappa_y$ . Physically, this means that purely cylindrical deformations with zero

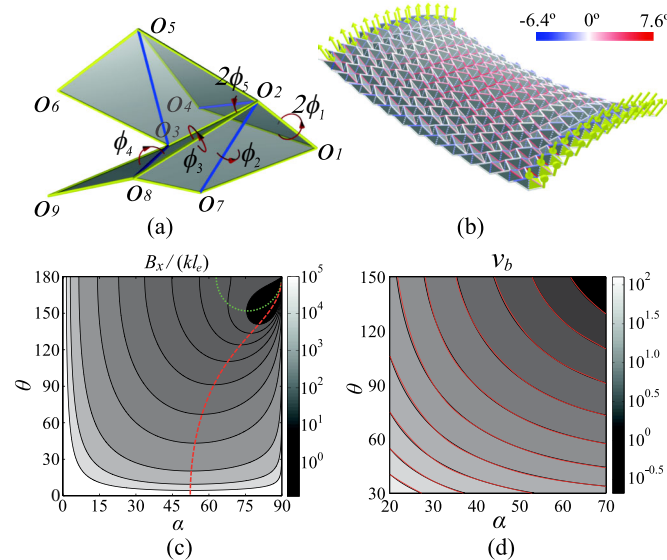


FIG. 3 (color online). Out-of-plane bending response of a unit cell. (a) The plaquettes deformations about each fold are symmetric about the plane  $O_1O_2O_3$ , so that the angles  $2\phi_1, \phi_2, \phi_3, \phi_4$ , and  $2\phi_5$  correspond to rotations about the axes  $\vec{O_1O_2}$ ,  $\vec{O_7O_2}$ ,  $\vec{O_2O_8}$ ,  $\vec{O_8O_3}$ , and  $\vec{O_3O_2}$ , respectively. (b) Numerical simulation of the bending of a Miura-ori plate with  $\alpha = 45^\circ$  and  $\theta = 90^\circ$ . Force dipoles are shown by yellow arrows. Color of the folds indicates the value of deformation angles. (c) Contour plot of dimensionless bending stiffness  $B_x/(kl_e)$  corresponding to pure bending of a unit cell. The green dotted curve and red dashed curve indicate the optimal design angle pairs that correspond to the local minima of  $B_x|_\alpha$  and  $B_x|_\theta$ , respectively. (d) Contour plot of bending Poisson's ratio. The gray scale plot is from the analytic expression (6) and the red curves are extracted from simulation results. In our simulations, we use a plate made of 21 by 21 unit cells and vary  $\alpha$  from  $20^\circ$  to  $70^\circ$ ,  $\theta$  from  $30^\circ$  to  $150^\circ$  both every  $10^\circ$ .



Gaussian curvature are impossible, as locally the unit cell can only be bent into a saddle with negative Gaussian curvature. In the continuum limit, this implies that the effective stiffness matrix [24] of a two-dimensional Miura-ori plate is singular, and has rank one. Thus, the two-dimensional deformations of a Miura plate can be described completely by a one-dimensional beam theory.

To calculate the bending stiffness per unit width of a single cell in the  $x$  direction  $B_x$ , we note that the elastic energy is physically stored in the eight discrete folds [Fig. 3(a)] and thus, is expressed as  $kl_e(2\phi_1^2 + \phi_3^2 + 2\phi_5^2) + 2k_p l_e \sin(\alpha/2)(\phi_4^2 + \phi_2^2)$ , where  $k$  and  $k_p$  are the spring constants of the ridges and the diagonal folds of plaquettes, respectively. In an effective continuum theory, the energy associated with the deformations of the unit cell when bent into a sheet may be described in terms of its curvatures. Thus, associated with the curvature  $\kappa_x$ , the energy per unit area of the sheet is  $(1/2)B_x w l \kappa_x^2$ , where the effective bending stiffness  $B_x$  is derived by equating the discrete and continuous versions of the energy and inserting  $w$ ,  $l$  from (1) and  $\kappa_x$  from (5). In general,  $B_x$  depends on multiple independent deformation angles, but we start by studying the “pure bending” case, where a row of unit cells aligned in the  $x$  direction undergo the same deformation and stretching is constrained, i.e.,  $\phi_1 = 0$  for all cells so that  $\phi_2 = \phi_4$ . In this well-defined limit,  $\phi_3 = (1/2)\phi_2 \csc(\alpha/2)[1 - 2\cos\alpha/(1 - \xi^2)]$  and  $\phi_5 = (1/2)\phi_2 \csc(\alpha/2)$ , so that

$$B_x(\alpha, \theta) = kl_e \left[ 2 + 16 \frac{k_p}{k} \sin^3 \frac{\alpha}{2} + \left( 1 - \frac{2\cos\alpha}{1 - \xi^2} \right)^2 \right] \times \cot\left(\frac{\theta}{2}\right) \frac{(1 - \xi^2)^{3/2}}{2\xi^2 \cos\alpha \sin\alpha \cos(\theta/2)}. \quad (7)$$

The bending stiffness per unit width of a single cell in the  $y$  direction  $B_y$  is related to  $B_x$  via the expression for bending Poisson’s ratio  $\nu_b^2 = B_x/B_y$ , where  $\nu_b$  is defined in (6). Just as there are optimum design parameters that allow us to extremize the in-plane rigidities, we can also find the optimal design angle pairs that minimize  $B_x$ , by setting  $\partial_\theta B_x|_\alpha = 0$  and  $\partial_\alpha B_x|_\theta = 0$ . This gives us two curves  $\theta_m(\alpha)$  and  $\alpha_m(\theta)$  shown in Fig. 3(c), where we have assumed  $k = k_p$ . To understand the bounds on  $B_x$ , we expand (7) in the vicinity of the extreme values of the design variables  $\alpha$  and  $\theta$  and find that  $B_x|_{\alpha \rightarrow 0} \sim \alpha^{-3}$ ,  $B_x|_{\alpha \rightarrow \pi/2} \sim (\pi/2 - \alpha)^{-1}$ , and  $B_x|_{\theta \rightarrow 0} \sim \theta^{-3}$ . We see that  $B_x|_{\theta \rightarrow \pi}$  is bounded except when  $(\alpha, \theta) = (\pi/2, \pi)$ , corresponding to the case of an almost flat, unfolded orthogonal Miura sheet. Given the geometric relation between  $B_x$  and  $B_y$ , we note that optimizing  $B_y$  is tantamount to extremizing  $B_x$ .

The deformation response of a complete Miura-ori plate requires a numerical approach because it is impossible to assemble an entire bent plate by periodically aligning unit cells with identical bending deformations in both the  $x$  and  $y$

directions. Our numerical model takes the form of a simple triangular-element based discretization of the sheet, in which each edge is treated as a linear spring with stiffness inversely proportional to its rest length. Each pair of adjacent triangles is assigned an elastic hinge with a bending energy quadratic in its deviation from an initial rest angle that is chosen to reflect the natural shape of the Miura-ori plate. We compute the elastic stretching forces and bending torques in a deformed mesh [25,26], assigning a scaled stretching stiffness that is six orders of magnitude larger than the bending stiffness of the adjacent facets, so that we may deform the mesh nearly isometrically. When our numerical model of a Miura-ori plate is bent by applied force dipoles along its left-right boundaries, it deforms into a saddle [Fig. 3(b)]. In this state, asymmetric inhomogeneous twisting arises in most unit cells; indeed this is the reason for the failure of averaging for this problem, since different unit cells deform differently, and we cannot derive an effective theory by considering just the unit cell. This is in contrast with the in-plane case, where the deformations of the unit cell are affinely related to those of the entire plate. Our results also show that the maximal stresses typically arise in the middle of the Miura-ori plate, away from boundaries. Thus, in a real plate, the vertices and hinges near the center are likely to fail first unless they are reinforced.

We now compare our predictions for the bending Poisson’s ratio  $\nu_b$  of the one-dimensional beam theory with those determined using full two-dimensional simulations. In Fig. 3(d), we plot  $\nu_b$  from (6) (the gray scale contour plot) based on a unit cell and  $\nu_b$  extracted at the center of the bent Miura-ori plate from simulations (the red curves). In the center of the plate where only symmetric bending and in-plane stretching modes are activated, the two approaches agree, but away from the center where this symmetry is violated, this is no longer true.

Folded structures, mechanical metamaterials might be named Orikozo, from the Japanese for folded matter. Our analysis of the simplest of these structures is rooted in the geometry of the unit cell as characterized by a pair of design angles  $\alpha$  and  $\theta$  together with the constraint of piecewise isometric deformations. We have found simple expressions for the linearized planar stretching rigidities  $K_x$ ,  $K_y$ , and nonplanar bending rigidities  $B_x$  and  $B_y$ , and shown that the bending response of a plate can be described in terms of that of a one-dimensional beam. Furthermore, we find that the in-plane Poisson’s ratio  $\nu_{wl} < 0$ , while the out-of-plane bending Poisson ratio  $\nu_b > 0$ , an unusual combination that is not seen in simple materials, satisfying the general relation  $\nu_{wl} = -\nu_l$ , a consequence of geometry alone. Our analysis also allows us to pose and solve a series of design problems to find the optimal geometric parameters of the unit cell that lead to extrema of stretching and bending rigidities as well as contraction or expansion ratios of the system. This paves the way for the use of optimally designed Miura-ori patterns in three-dimensional nanostructure fabrication [27], and raises

the possibility of optimal control of actuated origami-based materials in soft robotics [28] and elsewhere using the simple geometrical mechanics approaches introduced here.

We thank the Wood lab for help with laser cutting the Miura-ori plates, the Wyss Institute and the Kavli Institute for support, and Tadashi Tokieda for discussions and the nomenclature Orikozo for these materials.

*Note added in proof.*—While our paper was under review, an experimental engineering study on foldable structures was published [29] consistent with our comprehensive theoretical and computational approach to the geometry and mechanics of Miura-ori.

---

\*lm@seas.harvard.edu

- [1] D. R. Smith, J. B. Pendry, and M. C. Wiltshire, *Science* **305**, 788 (2004).
- [2] G. N. Greaves, A. L. Greer, R. S. Lakes, and T. Rouxel, *Nat. Mater.* **10**, 823 (2011).
- [3] Wm. T. M. Forbes, *Psyche* **31**, 254 (1924).
- [4] H. Kobayashi, B. Kresling, and J. F. V. Vincent, *Proc. R. Soc. B* **265**, 147 (1998).
- [5] H. Kobayashi, M. Daimaruya, and H. Fujita, *Solid Mech. Its Appl.* **106**, 207 (2003).
- [6] K. Miura, in *Proceedings of 31st Congress International Astronautical Federation, Tokyo*, 1980, IAF-80-A 31:1-10.
- [7] E. A. Elsayed and B. B. Basily, *Int. J. Mater. Prod. Technol.* **21**, 217 (2004).
- [8] R. S. Lakes, *Science* **235**, 1038 (1987).
- [9] B. D. Caddock and K. E. Evans, *J. Phys. D* **22**, 1877 (1989); K. E. Evans and B. D. Caddock, *J. Phys. D* **22**, 1883 (1989).
- [10] A. Y. Haeri, D. J. Weidner, and J. B. Parise, *Science* **257**, 650 (1992).
- [11] A. L. Goodwin, D. A. Keen, and G. Tucker, *Proc. Natl. Acad. Sci. U.S.A.* **105**, 18 708 (2008).
- [12] K. E. Evans, M. A. Nkansah, J. Hutchinson, and S. C. Rogers, *Nature (London)* **353**, 124 (1991).
- [13] R. Lang, *Origami Design Secrets: Mathematical Methods for an Ancient Art* (A K Peters/CRC Press, Boca Raton, FL, 2011), 2nd ed.
- [14] E. Demaine and J. O'Rourke, *Geometric Folding Algorithms: Linkages, Origami, Polyhedra* (Cambridge University Press, Cambridge, England, 2007).
- [15] T. Hull, *Project Origami: Activities for Exploring Mathematics* (A K Peters/CRC Press, Boca Raton, FL, 2011).
- [16] Y. Klettand and K. Drechsler, in *Origami5: International Meeting of Origami, Science, Mathematics, and Education*, edited by P. Wang-Iverson, R. J. Lang, and M. Yim (CRC Press, Boca Raton, FL, 2011), pp. 305–322.
- [17] M. Schenk and S. Guest, in *Origami5: International Meeting of Origami, Science, Mathematics, and Education*, edited by P. Wang-Iverson, R. J. Lang, and M. Yim (CRC Press, Boca Raton, FL, 2011), pp. 291–304.
- [18] A. Papa and S. Pellegrino, *J. Spacecr. Rockets* **45**, 10 (2008).
- [19] N. Bowden, S. Brittain, A. G. Evans, J. W. Hutchinson, and G. M. Whitesides, *Nature (London)* **393**, 146 (1998).
- [20] L. Mahadevan and S. Rica, *Science* **307**, 1740 (2005).
- [21] B. Audoly and A. Boudaoud, *J. Mech. Phys. Solids* **56**, 2444 (2008).
- [22] See Supplemental Material at <http://link.aps.org/supplemental/10.1103/PhysRevLett.110.215501> for detailed derivations.
- [23] In general, the incremental Poisson's ratio is  $\nu_b = -d\kappa_y/d\kappa_x$ , but here, we only consider linear deformations about the flat state, so  $\nu_b = -\kappa_y/\kappa_x$ .
- [24] E. Ventsel and T. Krauthammer, *Thin Plates and Shells: Theory, Analysis, and Applications* (CRC Press, Boca Raton, FL, 2001), 1st ed., pp. 197–199.
- [25] R. Bridson, S. Marino, and R. Fedkiw, ACM SIGGRAPH/Eurograph. Symp. Comp. Animation (SCA) (2003), pp. 28–36.
- [26] R. Burgoon, E. Grinspun, and Z. Wood, in *Proceedings of the ISCA 21st International Conference on Computers and Their Applications*, (ISCA, 2006), p. 180.
- [27] W. J. Arora, A. J. Nichol, H. I. Smith, and G. Barbastathis, *Appl. Phys. Lett.* **88**, 053108 (2006).
- [28] E. Hawkes, B. An, N. Benbernou, H. Tanaka, S. Kim, E. D. Demaine, D. Rus, and R. J. Wood, *Proc. Natl. Acad. Sci. U.S.A.* **107**, 12 441 (2010).
- [29] M. Schenk and S. Guest, *Proc. Natl. Acad. Sci. U.S.A.* **110**, 3276 (2013).

# Supplementary Material for “Geometric Mechanics of Periodic Pleated Origami” by Wei et al.

March 23, 2013

## Contents

<b>1</b>	<b>Geometry and Kinematics</b>	<b>1</b>
<b>2</b>	<b>In-plane stretching response of a Miura-ori plate</b>	<b>4</b>
2.1	Poisson’s ratio related to height changes . . . . .	4
2.2	Stretching stiffness $K_x$ and $K_y$ . . . . .	4
2.3	Asymptotic cases for optimal design angles . . . . .	5
<b>3</b>	<b>Out-of-plane bending response of a Miura-ori plate</b>	<b>6</b>
3.1	Minimum model for isometric bending . . . . .	6
3.2	Curvatures and the bending Poisson’s ratio when short folds are introduced . . . . .	7
3.3	Curvatures and the bending Poisson’s ratio when long folds are introduced . . . . .	10
3.4	Bending stiffness $B_x$ and $B_y$ . . . . .	11
3.5	Pure bending . . . . .	12
<b>4</b>	<b>Numerical simulations of the bending response of a Miura-ori plate</b>	<b>12</b>
4.1	Homogeneous deformation in bent plate is impossible . . . . .	12
4.2	Simulation model . . . . .	12

## 1 Geometry and Kinematics

The unit cell of a Miura-ori patterned plate is shown in Fig.S.1 and is parameterized by two dihedral angles  $\theta \in [0, \pi]$ ,  $\beta \in [0, \pi]$ , and one oblique angle  $\alpha$ , in a unit cell of length  $l$ , width  $w$ , and height  $h$ . We treat the structure as being made of identical periodic rigid skew plaquettes joined by elastic hinges at the ridges. The structure can deploy uniformly in the plane by having each constituent skew plaquette in a unit cell rotate rigidly about the connecting elastic ridges. Then the ridge lengths  $l_1$ ,  $l_2$  and  $\alpha \in [0, \pi/2]$  are constant through folding/unfolding, so that we may choose  $\theta$  (or equivalently  $\beta$ ) to be the only degree of freedom that completely characterizes a Miura-ori cell.

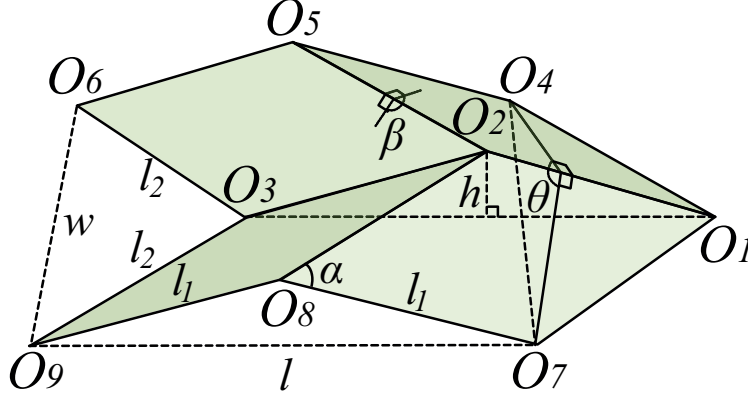


Figure S.1: Sketch of a unit cell of Miura Ori pattern.

The geometry of the unit cell implies that

$$\begin{aligned} \beta &= 2 \sin^{-1}(\zeta \sin(\theta/2)), \quad l = 2l_1\zeta, \\ w &= 2l_2\xi \quad \text{and} \quad h = l_1\zeta \tan \alpha \cos(\theta/2), \end{aligned} \quad (\text{S.1})$$

where the dimensionless width and height are

$$\xi = \sin \alpha \sin(\theta/2) \quad \text{and} \quad \zeta = \cos \alpha (1 - \xi^2)^{-1/2}. \quad (\text{S.2})$$

We see that  $\beta$ ,  $l$ ,  $w$ , and  $h$  change monotonically as  $\theta \in [0, \pi]$ , with  $\beta \in [0, \pi]$ ,  $l \in [2l_1 \cos \alpha, 2l_1]$ ,  $w \in [0, 2l_2 \sin \alpha]$ , and  $h \in [0, l_1 \sin \alpha]$ . As  $\alpha \in [0, \pi/2]$ , we see that  $\beta \in [\theta, 0]$ ,  $l \in [2l_1 \cos \alpha, 2l_1]$ ,  $w \in [0, 2l_2 \sin(\theta/2)]$  and  $h \in [0, l_1 \sin \alpha]$ .

Before we discuss the coupled deformations of the plate embodied functionally as  $\beta(\alpha, \theta)$ , we investigate the case when  $\alpha = \pi/2$  corresponding to an orthogonally folded map that can only be completely unfolded first in one direction and then another, without bending or stretching the sheet except along the hinges. Indeed, when  $\alpha = \pi/2$  and  $\theta \neq \pi$ , Eq. (S.1) reduces to  $\beta = 0$ ,  $l = 0$  and  $h = l_1$ , the singular limit when Miura-ori patterned sheets can not be unfolded with a single diagonal pull. Close to this limiting case, when the folds are almost orthogonal, the Miura-ori pattern can remain almost completely folded in the  $x$  direction ( $\beta$  changes only by a small amount) while unfolds in the  $y$  direction as  $\theta$  is varied over a large range, only to expand suddenly in the  $x$  direction at the last moment. This observation can be explained by expanding Eq. (S.1) asymptotically as  $\alpha \rightarrow \pi/2$  and  $\theta \rightarrow \pi$ , which yields  $\beta \approx \pi - \epsilon/\delta$ ,  $l \approx l_1(2 - (\epsilon/\delta)^2/4)$ ,  $w \approx l_2(2 - \delta^2 - \epsilon^2/4)$  and  $h \approx l_1\epsilon/(2\delta)$ , where  $\delta = \pi/2 - \alpha$  and  $\epsilon = \pi - \theta$ . Thus, we see that for any fixed small constant  $\delta$ , only when  $\epsilon < \delta$ , do we find that  $\beta \rightarrow \pi$ ,  $l \rightarrow 2l_2$  and  $h \rightarrow 0$ , leading to a sharp transition in the narrow neighborhood ( $\sim \delta$ ) of  $\theta = \pi$  as  $\alpha \rightarrow \pi/2$  (Fig.S.2a), consistent with our observations.

More generally, we start by considering the volumetric packing of Miura-ori characterized by the effective volume of a unit cell  $V \equiv l \times w \times h = 2l_1^2 l_2 \zeta^2 \sin \theta \sin \alpha \tan \alpha$ , which vanishes when  $\theta = 0, \pi$ . To determine the conditions when the volume is at an extremum for a fixed in-plane angle  $\alpha$ , we set  $\partial_\theta V|_\alpha = 0$  and find that the maximum volume

$$V_{max}|_\alpha = 2l_1^2 l_2 \sin^2 \alpha \quad \text{at} \quad \theta_m = \cos^{-1} \left( \frac{\cos 2\alpha - 1}{\cos 2\alpha + 3} \right), \quad (\text{S.3})$$

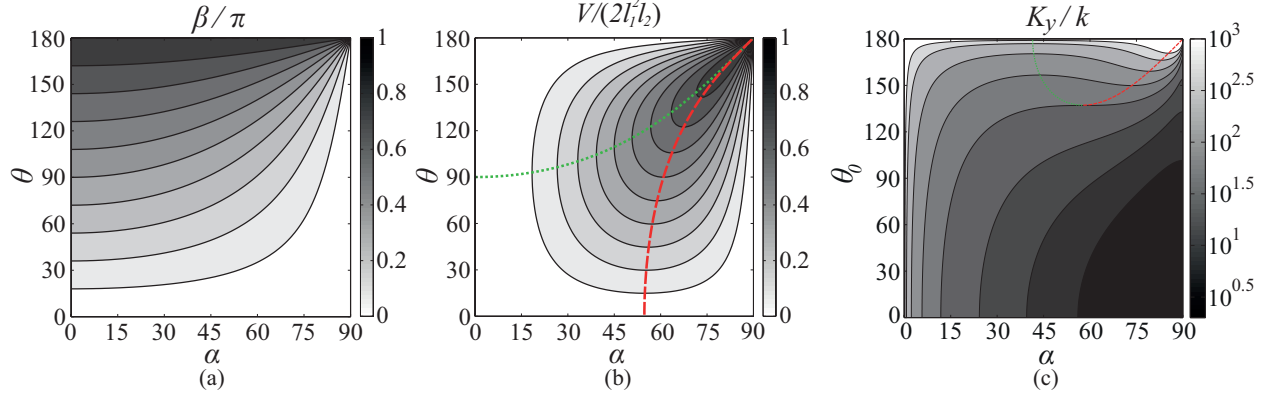


Figure S.2: Geometry of the unit cell as a function of  $\alpha$  and  $\theta$ . (a) The folding angle  $\beta$  increases as  $\theta$  increases and decreases as  $\alpha$  increases. The transition becomes sharper as  $\alpha \approx \pi/2$ , and when  $\alpha = \pi/2$ ,  $\beta = 0$  independent of  $\theta$ , i.e. the unfolding (folding) of folded (unfolded) of maps with  $N$  orthogonal folds has  $2^N$  decoupled possibilities. (b) Effective dimensionless volume  $V/(2l_1^2l_2)$ . The green dotted curve  $\theta_m(\alpha)$  indicates the optimal design angle pairs that correspond to the maximum  $V|_\alpha$ . The red dashed curve  $\alpha_m(\theta)$  indicates the optimal design angle pairs that correspond to the maximum  $V|_\theta$ . (c) Contour plot of the dimensionless stretching rigidity  $K_y/k$ .  $K_y|_\alpha$  is monotonic in  $\theta_0$ . The green dotted curve indicates the design angle pairs that correspond to the minima of  $K_y|_{\theta_0}$ . The red dashed curve indicates the design angle pairs that correspond to the maxima of  $K_x|_{\theta_0}$ . See the text for details.

shown as a red dashed line in Fig.S.2b. Similarly, for a given dihedral angle  $\theta$ , we may ask when the volume is extremized as a function of  $\alpha$ ? Using the condition  $\partial_\alpha V|_\theta = 0$  shows that the maximum volume is given by

$$V_{max}|_\theta = \frac{4l_1^2l_2 \cos \alpha_m (\sqrt{5 + 4 \cos \theta} - 3) \cot^2 (\theta/2) \sin \theta}{\sqrt{5 + 4 \cos \theta} - 3 - 2 \cos \theta} \quad (\text{S.4})$$

at

$$\alpha_m = \cos^{-1} \left[ \sqrt{\left(2 + \cos \theta - \sqrt{5 + 4 \cos \theta}\right) / (\cos \theta - 1)} \right],$$

shown as a red dashed line in Fig.S.2b. These relations for the maximum volume as a function of the two angles that characterize the Miura-ori allow us to manipulate the configurations for the lowest density in such applications as packaging for the best protection. In the following sections, we assume each plaquette is a rhombus, i.e.  $l_1 = l_2 = l_e$ , to keep the size of the algebraic expressions manageable, although it is a relatively straightforward matter to account for variations from this limit.



## 2 In-plane stretching response of a Miura-ori plate

### 2.1 Poisson's ratio related to height changes

Poisson's ratios related to height changes,  $\nu_{hl}$  and  $\nu_{wl}$  read

$$\begin{aligned}\nu_{hl} &= \nu_{lh}^{-1} \equiv -\frac{dh/h}{dl/l} = \cot^2 \alpha \sec^2 \frac{\theta}{2}, \\ \nu_{hw} &= \nu_{wh}^{-1} \equiv -\frac{dh/h}{dw/w} = \zeta^2 \tan^2 \frac{\theta}{2}.\end{aligned}\tag{S.5}$$

which are both positive, and monotonically increasing with  $\theta$  and  $\alpha$ . Expansion of  $\nu_{hl}$  in Eq. (S.5) shows that  $\nu_{hl}|_{\theta \rightarrow \pi} \sim (\pi - \theta)^{-2}$  and thus  $\nu_{hl}|_{\alpha} \in [\cot^2 \alpha, \infty)$ , while  $\nu_{hl}|_{\alpha \rightarrow 0} \sim \alpha^{-2}$  and thus  $\nu_{hl}|_{\theta} \in (\infty, 0]$ . Similarly, expansion of  $\nu_{hw}$  in Eq. (S.5) shows that  $\nu_{hw}|_{\theta \rightarrow \pi} \sim (\pi - \theta)^{-2}$  and thus  $\nu_{hw}|_{\alpha} \in [0, \infty)$ , while  $\nu_{hw}|_{\theta} \in [\tan^2(\theta/2), 0]$ . Finally, it is worth pointing out that  $\nu_{hw}$  has a singularity at  $(\alpha, \theta) = (\pi/2, \pi)$ .

### 2.2 Stretching stiffness $K_x$ and $K_y$

Here we derive the expressions for stretching stiffness  $K_x$  and  $K_y$ .

The expression for the potential energy of a unit cell deformed by a uniaxial force  $f_x$  in the  $x$  direction is given by

$$H = U - \int_{\theta_0}^{\theta} f_x \frac{dl}{d\theta'} d\theta',\tag{S.6}$$

where the unit cell length  $l$  is defined in Eq. (S.1). The elastic energy of a unit cell  $U$  is stored only in the elastic hinges which allow the plaquettes to rotate, and is given by

$$U = kl_e(\theta - \theta_0)^2 + kl_e(\beta - \beta_0)^2,\tag{S.7}$$

where  $k$  is the hinge spring constant, and  $\theta_0$  and  $\beta_0 (= \beta(\alpha, \theta_0))$  are the natural dihedral angles in the undeformed state. The external force  $f_x$  at equilibrium state is obtained using the condition that the first variation  $\delta H/\delta \theta = 0$ , which reads

$$f_x = \frac{dU/d\theta}{dl/d\theta} = 2k \frac{(\theta - \theta_0) + (\beta - \beta_0)\varpi(\alpha, \theta)}{\eta(\alpha, \theta)},\tag{S.8}$$

where  $U$  is defined in Eq. (S.7),  $l$  is defined in Eq. (S.1), and in addition

$$\varpi(\alpha, \theta) = \frac{\cos \alpha}{1 - \xi^2} \quad \text{and} \quad \eta(\alpha, \theta) = \frac{\cos \alpha \sin^2 \alpha \sin \theta}{2(1 - \xi^2)^{3/2}}.\tag{S.9}$$

The stretching rigidity associated with the  $x$  direction is thus given by

$$K_x(\alpha, \theta_0) \equiv \left. \frac{df_x}{d\theta} \right|_{\theta_0} = 4k \frac{(1 - \xi_0^2)^2 + \cos^2 \alpha}{(1 - \xi_0^2)^{\frac{1}{2}} \cos \alpha \sin^2 \alpha \sin \theta_0},\tag{S.10}$$

where  $\xi_0 = \xi(\alpha, \theta_0)$ .

Similarly, the uniaxial force in the  $y$  direction in a unit cell at equilibrium is

$$f_y = \frac{dU/d\theta}{dw/d\theta} = 2k \frac{(\theta - \theta_0) + (\beta - \beta_0)\varpi(\alpha, \theta)}{\sin \alpha \cos(\theta/2)}, \quad (\text{S.11})$$

where  $w$  is defined in Eq. (S.1) and  $\varpi$  is defined in Eq. (S.9). The stretching rigidity in  $y$  direction is thus given by

$$K_y(\alpha, \theta_0) \equiv \left. \frac{df_y}{d\theta} \right|_{\theta_0} = 2k \frac{(1 - \xi_0^2)^2 + \cos^2 \alpha}{(1 - \xi_0^2)^2 \sin \alpha \cos(\theta_0/2)}, \quad (\text{S.12})$$

of which the contour plot is show in Fig. S.2c.

### 2.3 Asymptotic cases for optimal design angles

The expressions in Section 2.2 allow us to derive in detail all the asymptotic cases associated with the optimal pairs of design angles which correspond to the extrema of stretching rigidities  $K_x$  and  $K_y$ . For simplicity, we use  $(\alpha, \theta)$  instead of  $(\alpha, \theta_0)$  to represent the design angle pairs when the unit cell is at rest.

1. Expanding  $\partial_\theta K_x$  in the neighborhood of  $\alpha = 0$  yields

$$\partial_\theta K_x|_{\alpha \rightarrow 0} = -\frac{8 \cot \theta \csc \theta}{\alpha^2} - \frac{2}{3} ((3 + \cos \theta) \csc^2 \theta) + O(\alpha^2). \quad (\text{S.13})$$

As  $\alpha \rightarrow 0$ ,  $\theta \rightarrow \pi/2$  to prevent a divergence. Continuing to expand Eq. (S.13) in the neighborhood of  $\theta = \pi/2$  and keeping the first two terms yields

$$\partial_\theta K_x|_{\theta \rightarrow \pi/2} = 0 \Rightarrow 4(\theta - \pi/2) = \alpha^2. \quad (\text{S.14})$$

Therefore in the contour plot of  $K_x$  (Fig.3b in the main text), the greed dotted curve is approximated by  $4(\theta - \pi/2) = \alpha^2$  in the neighborhood of  $\alpha = 0$ , and is perpendicular to  $\alpha = 0$  as  $\theta$  is quadratic in  $\alpha$ .

2. Expanding  $\partial_\alpha K_x$  in the neighborhood of  $\theta = 0$  yields

$$\begin{aligned} \partial_\alpha K_x|_{\theta \rightarrow 0} = & -\frac{[11 + 20 \cos(2\alpha) + \cos(4\alpha)] \csc^3 \alpha \sec^2 \alpha}{2\theta} - \frac{1}{192} \{[290 + 173 \cos(2\alpha) \\ & + 46 \cos(4\alpha) + 3 \cos(6\alpha)] \csc^3 \alpha \sec^2 \alpha\} \theta + O(\theta^2). \end{aligned} \quad (\text{S.15})$$

The numerator of the leading order in Eq. (S.15) has to vanish as  $\theta \rightarrow 0$  to keep the result finite, which results in a unique solution  $\alpha^* = \cos^{-1}(\sqrt{\sqrt{5} - 2})$  in the domain  $\alpha \in (0, \pi/2)$ . Continuing to expand Eq. (S.15) in the neighborhood of  $\alpha = \alpha^*$  and only keeping the first two terms yields

$$\partial_\alpha K_x = 0|_{\alpha \rightarrow \alpha^*} \Rightarrow 4\sqrt{5(1 + \sqrt{5})}(\alpha - \alpha^*) = \theta^2. \quad (\text{S.16})$$

so the red dashed curve in the contour plot of  $K_x$  (Fig.3b in the main text) is perpendicular to  $\theta = 0$ .

3. Similarly, Expansion of  $\partial_\alpha K_y$  near  $\theta = \pi$  yields

$$\partial_\alpha K_y|_{\theta \rightarrow \pi} = \frac{[-1 + 16 \cos(2\alpha) + \cos(4\alpha)] \csc^2 \alpha \sec^3 \alpha}{2(\theta - \pi)} + \frac{1}{192} [638 - 737 \cos(2\alpha) + 162 \cos(4\alpha) + \cos(6\alpha)] \csc^2 \alpha \sec^5 \alpha (\theta - \pi) + O[(\theta - \pi)^3]. \quad (\text{S.17})$$

Allowing for a well behaved limit at leading order as  $\theta \rightarrow \pi$  requires  $-1 + 16 \cos(2\alpha) + \cos(4\alpha) = 0$  and yields  $\alpha^* = \cos^{-1} \left( \sqrt{(\sqrt{17} - 3)/2} \right)$  as the unique solution when  $\alpha$  is an acute. Again expanding Eq. (S.17) in the neighborhood of  $\theta = \pi$ , and only keeping the first two terms yields

$$\partial_\alpha K_y|_{\alpha \rightarrow \alpha^*} = 0 \Rightarrow 2\sqrt{1 + \sqrt{17}}(\alpha_m - \alpha^*) = (\pi - \theta)^2. \quad (\text{S.18})$$

So the green dotted curve in the contour plot of  $K_y$  (Fig. S.2c) is approximated by  $2\sqrt{1 + \sqrt{17}}(\alpha_m - \alpha^*) = (\pi - \theta)^2$  near  $\alpha = \alpha^*$ , and is perpendicular to  $\theta = \pi$ . The point where the green curve ends satisfies the condition

$$\partial_\alpha K_y = 0 \quad \text{and} \quad \partial_\alpha (\partial_\alpha K_y) = 0 \quad (\text{S.19})$$

and numerical calculation gives us the coordinates of this critical point as

$$\theta = 2.39509, \quad \text{and} \quad \alpha = 1.00626. \quad (\text{S.20})$$

The red dashed curve (Fig. S.2c) starting at this point shows a collection of optimal design angle pairs  $(\alpha, \theta)$  where  $K_y|_\theta$  is locally maximal.

### 3 Out-of-plane bending response of a Miura-ori plate

#### 3.1 Minimum model for isometric bending

Here we show that planar folding is the only geometrically possible motion under the assumption that the unit cell deforms isometrically, i.e. with only rotations of the rhombus plaquettes about the hinges. To enable the out-of-plane bending mode, the minimum model for isometric deformations requires the introduction of 1 additional diagonal fold into each plaquette, and this follows from the explanation below.

Suppose the plane  $O_1O_2O_5O_4$  (Fig.S.3a) is fixed to eliminate all rigid motions, for any dihedral angle  $\theta$ , the orientation of plane  $O_1O_2O_8O_7$  is determined. However, the other two rhombi  $O_2O_5O_6O_3$  and  $O_2O_3O_9O_8$  are free to rotate about axis  $O_2O_5$  and  $O_2O_8$  respectively and sweep out two cones which intersect at  $O_2O_3$  and  $O_2O'_3$ . Fig.S.3a shows the two possible configurations of a unit cell determined from the two intersections, the yellow part being the red part that has been flipped about a plane of symmetry. The unit cell in red is the only nontrivial Miura pattern, so that for any given  $\theta$ , there is a unique configuration of the unit cell corresponding to it. Any continuous change in  $\theta$  results in the unit cell being expanded or folded but remaining planar, in which case,  $O_1, O_4, O_7, O_3, O_6$  and  $O_9$  also remain coplanar. In order to enable the bending mode of the unit cell, the planarity of each plaquette must be violated. In the limit where the plaquette thickness  $t \ll 1$  the stretching rigidity ( $\sim t$ ) is much larger than the bending rigidity ( $\sim t^3$ ), with  $t$  being the thickness of a plaquette, while the energy required to bend a strip of ridge is 5 times of that

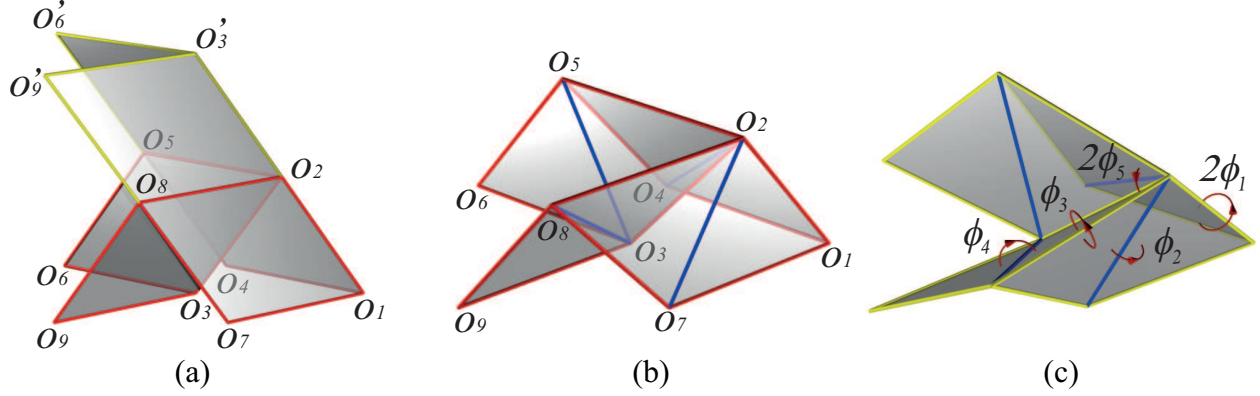


Figure S.3: Bending of a unit cell. (a) The two configurations of a unit cell for any given  $\theta$  if each plaquette is a rigid rhombus. The only possible motion is in-plane stretching. The yellow plaquettes illustrate the trivial configuration of two rigid plaquettes and the red ones show the typical configuration of a Miura-ori unit cell. (b) The undeformed state. An additional fold along the short diagonal is introduced to divide each rhombus into 2 elastically hinged triangles. (c) Symmetrically bent state. The bending angles around axis  $\overrightarrow{O_2O_4}$  and  $\overrightarrow{O_3O_5}$  are the same as those around  $\overrightarrow{O_7O_2}$  and  $\overrightarrow{O_8O_3}$  respectively.

required to stretch it according to the asymptotic analysis of the *Föppl – von Kármán* equations [1]. Therefore, the rigid ridge/fold is an excellent approximation for out-of-plane bending when  $t \ll 1$ . Then, to get a bent shape in a unit cell and thence in a Miura-ori plate, we must introduce an additional fold into each rhombus to divide it into two elastically hinged triangles (Fig.S.3b). As a result, 4 additional degrees of freedom are introduced in each unit cell. The deformed state can either be symmetrical about the plane  $O_1O_2O_3$  (Fig.S.3c) corresponding to a bending mode, or unsymmetrical corresponding to a twisting mode. Here, we are only interested in the bent state, in which the rotation angle  $\phi_2$  about the axis  $\overrightarrow{O_2O_4}$ , and  $\phi_4$  about the axis  $\overrightarrow{O_3O_5}$ , are the same as the rotations about  $\overrightarrow{O_7O_2}$  and  $\overrightarrow{O_8O_3}$  respectively. The rotation angles about the axis  $\overrightarrow{O_1O_2}$ ,  $\overrightarrow{O_3O_2}$  and  $\overrightarrow{O_2O_5}$  are  $2\phi_1$ ,  $2\phi_5$  and  $\phi_3$  respectively. ( $\rightarrow$  indicates the direction.)

### 3.2 Curvatures and the bending Poisson's ratio when short folds are introduced

Here we derive expressions for the coordinates of every vertex of the unit cell after bending in the linear deformation regime, from which curvatures in the two principle directions  $\kappa_x$ ,  $\kappa_y$  and the bending Poisson's ratio  $\nu_b = -\kappa_y/\kappa_x$  can be calculated.

To do so, we first need to know the transformation matrix associated with rotation about an arbitrary axis. The rotation axis is defined by a point  $\{a, b, c\}$  that it goes through and a direction vector  $\langle u, v, w \rangle$ , where  $u, v, w$  are directional cosines. Suppose a point  $\{x_0, y_0, z_0\}$  rotates about this axis by an infinitesimal small angle  $\omega$  ( $\omega \ll 1$ ), and reaches the new position  $\{x, y, z\}$ . Keeping only the leading order terms of the transformation matrix, we find that the new position  $\{x, y, z\}$

is given by

$$\begin{aligned}x &= x_0 + (-cv + bw - wy_0 + vz_0)\omega, \\y &= y_0 + (cu - aw + wx_0 - uz_0)\omega, \\z &= z_0 + (-bu + av - vx_0 + uy_0)\omega.\end{aligned}\tag{S.21}$$

Given Eq. (S.21), we are ready to calculate the coordinates of all vertices in the bent state. Assuming that the origin is at  $O_2$ , in the undeformed unit cell, edge  $O_1O_2$  is fixed in  $xoz$  plane to eliminate rigid motions. Each fold deforms linearly by angle  $2\phi_1$ ,  $\phi_2$ ,  $\phi_3$ ,  $\phi_4$  and  $2\phi_5$  (see Fig. S.3c) around corresponding axes respectively. The coordinates of  $O_1$  and  $O_2$  are

$$\begin{aligned}O_{1x} &= \frac{\cos \alpha}{\sqrt{1 - \xi^2}}, \quad O_{1y} = 0, \quad O_{1z} = -\frac{\sin \alpha \cos(\theta/2)}{\sqrt{1 - \xi^2}}; \\O_{2x} &= 0, \quad O_{2y} = 0, \quad O_{2z} = 0.\end{aligned}\tag{S.22}$$

The coordinates of  $O_3$  after bending are

$$\begin{aligned}O_{3x} &= -\frac{\cos \alpha}{\sqrt{1 - \sin^2 \alpha \sin^2(\theta/2)}} - \frac{\cos(\alpha/2) \sin \alpha \sin \theta}{\sqrt{3 - \cos(2\alpha)(\cos \theta - 1) + \cos \theta}}\phi_2 + \frac{\sin^2 \alpha \sin \theta}{2\sqrt{1 - \sin^2 \alpha \sin^2(\theta/2)}}\phi_3, \\O_{3y} &= -\frac{4 \cos(\theta/2) \sin(2\alpha)}{3 + \cos(2\alpha) + 2 \cos \theta \sin^2 \alpha}\phi_1 + \frac{\csc(\theta/2)[- \sin \alpha + \sin(2\alpha) + \sin^3 \alpha \sin^2(\theta/2)] \sin \theta}{[3 + \cos(2\alpha) + 2 \cos(\theta) \sin^2 \alpha] \sin(\alpha/2)}\phi_2 \\&\quad + \cos(\theta/2) \sin(\alpha) \phi_3, \\O_{3z} &= -\frac{\cos(\theta/2) \sin \alpha}{\sqrt{1 - \sin^2 \alpha \sin^2(\theta/2)}} + \frac{2 \cos \alpha \cos(\alpha/2) \sin(\theta/2)}{\sqrt{3 - \cos(2\alpha)(\cos \theta - 1) + \cos \theta}}\phi_2 - \frac{\cos \alpha \sin \alpha \sin(\theta/2)}{\sqrt{1 - \sin^2 \alpha \sin^2(\theta/2)}}\phi_3.\end{aligned}\tag{S.23}$$

The coordinates of  $O_4$  after bending are

$$\begin{aligned}O_{4x} &= \frac{\cos \alpha + \sin^2 \alpha \sin^2(\theta/2) - 1}{\sqrt{1 - \sin^2 \alpha \sin^2(\theta/2)}} - \frac{\sin^2 \alpha \sin \theta}{\sqrt{3 - \cos(2\alpha)(\cos \theta - 1) + \cos \theta}}\phi_1, \\O_{4y} &= \sin \alpha \sin(\theta/2) - \cos(\theta/2) \sin \alpha \phi_1, \\O_{4z} &= -\frac{\cos(\theta/2) \sin \alpha}{\sqrt{1 - \sin^2 \alpha \sin^2(\theta/2)}} - \frac{2 \cos \alpha \sin \alpha \sin(\theta/2)}{\sqrt{3 - \cos(2\alpha)(\cos \theta - 1) + \cos \theta}}\phi_1.\end{aligned}\tag{S.24}$$

The coordinates of  $O_5$  after bending are

$$\begin{aligned}O_{5x} &= -\sqrt{1 - \sin^2 \alpha \sin^2(\theta/2)} - \frac{\sin^2 \alpha \sin \theta}{\sqrt{3 - \cos(2\alpha)(\cos \theta - 1) + \cos \theta}}\phi_1 \\&\quad + \frac{\sin^2 \alpha \sin \theta}{2\sqrt{3 - \cos(2\alpha)(\cos \theta - 1) + \cos \theta} \sin(\alpha/2)}\phi_2, \\O_{5y} &= \sin \alpha \sin(\theta/2) - \cos(\theta/2) \sin \alpha \phi_1 + \frac{\cos(\theta/2) \sin \alpha}{2 \sin(\alpha/2)}\phi_2, \\O_{5z} &= -\frac{2 \cos \alpha \sin \alpha \sin(\theta/2)}{\sqrt{3 - \cos(2\alpha)(\cos \theta - 1) + \cos \theta}}\phi_1 + \frac{\cos \alpha \sin \alpha \sin(\theta/2)}{\sqrt{3 - \cos(2\alpha)(\cos \theta - 1) + \cos \theta} \sin(\alpha/2)}\phi_2.\end{aligned}\tag{S.25}$$



The coordinates of  $O_6$  after bending are

$$\begin{aligned}
O_{6x} &= \frac{\sin^2 \alpha \sin^2(\theta/2) - \cos \alpha - 1}{\sqrt{1 - \sin^2 \alpha \sin^2(\theta/2)}} - \frac{\sin^2 \alpha \sin \theta}{\sqrt{3 - \cos(2\alpha)(\cos \theta - 1) + \cos \theta}} \phi_1 \\
&\quad + \frac{\sin^2 \alpha \sin \theta}{2\sqrt{1 - \sin^2 \alpha \sin^2(\theta/2)}} \phi_3 - \frac{\sin \alpha \sin \theta \cos(\alpha/2)}{\sqrt{3 - \cos(2\alpha)(\cos \theta - 1) + \cos \theta}} \phi_4, \\
O_{6y} &= \sin \alpha \sin(\theta/2) + \frac{4 \cos(\theta/2) \sin \alpha [\sin^2 \alpha \sin^2(\theta/2) - 1 - 2 \cos \alpha]}{3 + \cos(2\alpha) + 2 \cos \theta \sin^2 \alpha} \phi_1 \\
&\quad + \frac{8 \cos \alpha \cos(\theta/2) \cos(\alpha/2)}{3 + \cos(2\alpha) + 2 \cos \theta \sin^2 \alpha} \phi_2 + \cos(\theta/2) \sin \alpha \phi_3 - \cos(\theta/2) \cos(\alpha/2) \phi_4, \\
O_{6z} &= -\frac{\cos(\theta/2) \sin \alpha}{\sqrt{1 - \sin^2 \alpha \sin^2(\theta/2)}} - \frac{2 \cos \alpha \sin \alpha \sin(\theta/2)}{\sqrt{3 - \cos(2\alpha)(\cos \theta - 1) + \cos \theta}} \phi_1 \\
&\quad + \frac{\csc(\alpha/2) \sin(2\alpha) \sin(\theta/2)}{\sqrt{3 - \cos(2\alpha)(\cos \theta - 1) + \cos \theta}} \phi_2 - \frac{\cos \alpha \sin \alpha \sin(\theta/2)}{\sqrt{1 - \sin^2 \alpha \sin^2(\theta/2)}} \phi_3 \\
&\quad + \frac{2 \cos \alpha \cos(\alpha/2) \sin(\theta/2)}{\sqrt{3 - \cos(2\alpha)(\cos \theta - 1) + \cos \theta}} \phi_4.
\end{aligned} \tag{S.26}$$

The coordinates of  $O_7$ ,  $O_8$  and  $O_9$  after bending are

$$\begin{aligned}
\{O_{7x}, O_{7y}, O_{7z}\} &= \{O_{4x}, -O_{4y}, O_{4z}\}, \quad \{O_{8x}, O_{8y}, O_{8z}\} = \{O_{5x}, -O_{5y}, O_{5z}\}, \\
\{O_{9x}, O_{9y}, O_{9z}\} &= \{O_{6x}, -O_{6y}, O_{6z}\}.
\end{aligned} \tag{S.27}$$

Due to symmetry,  $O_3$  must lie in the  $xoz$  plane after bending, so  $O_{3y} = 0$ , from which  $\phi_3$  and  $\phi_5$  can be expressed as a function of  $\phi_1$  and  $\phi_2$ ,

$$\begin{aligned}
\phi_3 &= \frac{8 \cos \alpha}{3 + \cos(2\alpha) + 2 \cos \theta \sin^2 \alpha} \phi_1 + \frac{1}{2} \csc\left(\frac{\alpha}{2}\right) \left(1 - \frac{8 \cos \alpha}{3 + \cos(2\alpha) + 2 \cos \theta \sin^2 \alpha}\right) \phi_2, \\
\phi_5 &= \phi_1 - \frac{1}{2} \csc\left(\frac{\alpha}{2}\right) \phi_2
\end{aligned} \tag{S.28}$$

The curvature of the unit cell in the  $x$  direction is defined as the dihedral angle formed by rotating plane  $O_4O_1O_7$  to plane  $O_6O_3O_9$  projected onto the  $x$  direction over the unit length  $l$ . The sign of the angle follows the right-hand rule about the  $y$  axis. The dihedral angle between plane  $O_4O_1O_7$  and plane  $xoy$  is

$$\Omega_{417} = \frac{O_{4z} - O_{1z}}{\sqrt{1 - \xi^2}} = -\frac{4 \cos \alpha \sin \alpha \sin(\theta/2)}{3 + \cos(2\alpha) + 2 \cos \theta \sin^2 \alpha} \phi_1, \tag{S.29}$$

and the dihedral angle between plane  $O_3O_6O_9$  and plane  $xoy$  is

$$\Omega_{639} = \frac{O_{6z} - O_{3z}}{\sqrt{1 - \xi^2}} = \frac{2[\cos(\alpha/2) + \cos(3\alpha/2)][\phi_2 + \phi_4 - 2\phi_1 \sin(\alpha/2)] \sin(\theta/2)}{3 + \cos(2\alpha) + 2 \cos \theta \sin^2 \alpha}. \tag{S.30}$$

The curvature  $\kappa_x$  hence is

$$\kappa_x = \frac{\Omega_{639} - \Omega_{417}}{l} = \frac{(\phi_2 + \phi_4) \cos(\alpha/2) \sin(\theta/2)}{2\sqrt{1 - \xi^2}}. \tag{S.31}$$

The curvature of the unit cell in the  $y$  direction is defined as the dihedral angle between plane  $O_4O_5O_6$  and  $O_7O_8O_9$  projected onto the  $y$  direction over the unit cell width  $w$ , which is expressed as

$$\kappa_y = -\frac{2O_{5y} - O_{4y} - O_{3y}}{hw} = -\frac{1}{4}(\phi_2 + \phi_4) \csc\left(\frac{\alpha}{2}\right) \csc\alpha \csc\left(\frac{\theta}{2}\right) \sqrt{1 - \xi^2}. \quad (\text{S.32})$$

From Eq. (S.31) and Eq. (S.32), we can calculate the bending Poisson ratio, which is simplified to

$$\nu_b = -\frac{\kappa_y}{\kappa_x} = -1 + \csc^2\alpha \csc^2\left(\frac{\theta}{2}\right). \quad (\text{S.33})$$

### 3.3 Curvatures and the bending Poisson's ratio when long folds are introduced

In Fig.S.3, if we introduce the additional fold along the long diagonal, e.g.  $O_1O_5$ , instead of the short one, the unit cell can be bent too. In this case,  $\phi_2$  and  $\phi_4$  are bending angles around axis  $\overrightarrow{O_1O_5}$  and  $\overrightarrow{O_2O_6}$  respectively.  $O_1, O_2$  do not change as they are fixed, and coordinates of  $O_3$  after bending are

$$\begin{aligned} O_{3x} &= -\frac{\cos\alpha}{\sqrt{1 - \sin^2\alpha \sin^2(\theta/2)}} + \frac{\sin^2\alpha \sin\theta}{2\sqrt{1 - \sin^2\alpha \sin^2(\theta/2)}}\phi_3 - \frac{\sin\alpha \sin(\alpha/2) \sin\theta}{\sqrt{3 - \cos(2\alpha)(\cos\theta - 1) + \cos\theta}}\phi_4, \\ O_{3y} &= -\frac{4\cos(\theta/2) \sin(2\alpha)}{3 + \cos(2\alpha) + 2\cos\theta \sin^2\alpha}\phi_1 + \cos\left(\frac{\theta}{2}\right) \sin(\alpha)\phi_3 - \cos\left(\frac{\theta}{2}\right) \sin\left(\frac{\alpha}{2}\right)\phi_4, \\ O_{3z} &= -\frac{\cos(\theta/2) \sin(\alpha)}{\sqrt{1 - \sin^2\alpha \sin^2(\theta/2)}} - \frac{\cos\alpha \sin\alpha \sin(\theta/2)}{\sqrt{1 - \sin^2\alpha \sin^2(\theta/2)}}\phi_3 + \frac{2\cos\alpha \sin(\alpha/2) \sin(\theta/2)}{\sqrt{3 - \cos(2\alpha)(\cos\theta - 1) + \cos\theta}}\phi_4. \end{aligned} \quad (\text{S.34})$$

The coordinates of  $O_4$  after bending are

$$\begin{aligned} O_{4x} &= \frac{\cos\alpha - 1 + \sin^2\alpha \sin^2(\theta/2)}{\sqrt{1 - \sin^2\alpha \sin^2(\theta/2)}} - \frac{\sin^2\alpha \sin\theta}{\sqrt{3 - \cos(2\alpha)(\cos\theta - 1) + \cos\theta}} \left[ \phi_1 - \frac{1}{2} \sec\left(\frac{\alpha}{2}\right) \phi_2 \right], \\ O_{4y} &= \sin\alpha \sin(\theta/2) - \cos(\theta/2) \sin\alpha \phi_1 + \cos(\theta/2) \sin(\alpha/2) \phi_2, \\ O_{4z} &= -\frac{\cos(\theta/2) \sin\alpha}{\sqrt{1 - \sin^2\alpha \sin^2(\theta/2)}} - \frac{2\cos\alpha \sin(\theta/2) \sin(\alpha/2)}{\sqrt{3 - \cos(2\alpha)(\cos\theta - 1) + \cos\theta}} \left[ 2\cos\left(\frac{\alpha}{2}\right) \phi_1 - \phi_2 \right]. \end{aligned} \quad (\text{S.35})$$

The coordinates of  $O_5$  after bending are

$$\begin{aligned} O_{5x} &= -\sqrt{1 - \sin^2\alpha \sin^2\left(\frac{\theta}{2}\right)} - \frac{\sin^2\alpha \sin\theta}{\sqrt{3 - \cos(2\alpha)(\cos\theta - 1) + \cos\theta}}\phi_1, \\ O_{5y} &= \sin\alpha \sin(\theta/2) - \cos(\theta/2) \sin\alpha \phi_1, \\ O_{5z} &= -\frac{\sin(2\alpha) \sin(\theta/2)}{\sqrt{3 - \cos(2\alpha)(\cos\theta - 1) + \cos\theta}}\phi_1. \end{aligned} \quad (\text{S.36})$$

The coordinates of  $O_6$  after bending are

$$\begin{aligned}
O_{6x} &= \frac{\sin^2 \alpha \sin^2(\theta/2) - \cos \alpha - 1}{\sqrt{1 - \sin^2 \alpha \sin^2(\theta/2)}} - \frac{\sin^2 \alpha \sin \theta}{\sqrt{3 - \cos(2\alpha)(\cos \theta - 1) + \cos \theta}} \phi_1 + \frac{\sin^2 \alpha \sin \theta}{2\sqrt{1 - \sin^2 \alpha \sin^2(\theta/2)}} \phi_3, \\
O_{6y} &= \sin \alpha \sin \left( \frac{\theta}{2} \right) + \frac{4 \cos(\theta/2) \sin \alpha [-1 - 2 \cos \alpha + \sin^2 \alpha \sin^2(\theta/2)]}{3 + \cos(2\alpha) + 2 \cos \theta \sin^2 \alpha} \phi_1 + \cos \left( \frac{\theta}{2} \right) \sin \alpha \phi_3, \\
O_{6z} &= -\frac{\cos(\theta/2) \sin \alpha}{\sqrt{1 - \sin^2 \alpha \sin^2(\theta/2)}} - \frac{\sin(2\alpha) \sin(\theta/2)}{\sqrt{3 - \cos(2\alpha)(\cos \theta - 1) + \cos \theta}} \phi_1 - \frac{\cos \alpha \sin \alpha \sin(\theta/2)}{\sqrt{1 - \sin^2 \alpha \sin^2(\theta/2)}} \phi_3.
\end{aligned} \tag{S.37}$$

Using the same idea for the long fold case as we did for the short fold, we can also calculate the curvatures in the two principal directions and find that

$$\kappa_x = \frac{\Omega_{639} - \Omega_{417}}{l} = \frac{2 [\sin(\alpha/2) - \sin(3\alpha/2)] \sin(\theta/2)}{[3 + \cos(2\alpha) + 2 \cos \theta \sin^2 \alpha] l} (\phi_2 + \phi_4) = \frac{\sin(\alpha/2) \sin(\theta/2)}{2l_e \sqrt{1 - \xi^2}} (\phi_2 + \phi_4), \tag{S.38}$$

while

$$\kappa_y = -\frac{2O_{5y} - O_{4y} - O_{3y}}{hw} = -\frac{\sqrt{1 - \sin^2 \alpha \sin^2(\theta/2)}}{2 \cos(\alpha/2) w} (\phi_2 + \phi_4) = -\frac{\sqrt{1 - \xi^2}}{4l_e \cos(\alpha/2) \xi} (\phi_2 + \phi_4). \tag{S.39}$$

Therefore the bending Poisson ratio is

$$\nu_b = -\frac{\kappa_y}{\kappa_x} = -1 + \csc^2 \alpha \csc^2 \left( \frac{\theta}{2} \right), \tag{S.40}$$

which is the same as that of the case when the short folds are introduced.

### 3.4 Bending stiffness $B_x$ and $B_y$

We are now in a position to derive expressions for the bending stiffness  $B_x$  and  $B_y$ . On one hand, the bending energy is physically stored in the 8 discrete folds, which can be expressed as  $1/2kl_e[4\phi_1^2 + 4\sin(\alpha/2)\phi_2^2 + 2\phi_3^2 + 4\sin(\alpha/2)\phi_4^2 + 4\phi_5^2]$ . On the other hand from a continuum point of view, the energy may also be effectively considered as stored in the entire unit cell that is bent into the curvature  $\kappa_x$ , which can be expressed as  $1/2B_x w l \kappa_x^2$ . Equating the two expressions for the same energy, we can write  $B_x$  as

$$\begin{aligned}
B_x &= kl_e \frac{4\phi_1^2 + 4\frac{k_p}{k} \sin(\frac{\alpha}{2})\phi_2^2 + 2\phi_3^2 + 4\frac{k_p}{k} \sin(\frac{\alpha}{2})\phi_4^2 + 4\phi_5^2}{wl \kappa_x^2}, \\
&= kl_e \left[ 2 + 16\frac{k_p}{k} \sin^3 \frac{\alpha}{2} + \left( 1 - \frac{2 \cos \alpha}{1 - \xi^2} \right)^2 \right] \cot \left( \frac{\theta}{2} \right) \frac{(1 - \xi^2)^{3/2}}{2\xi^2 \cos \alpha \sin \alpha \cos(\theta/2)},
\end{aligned} \tag{S.41}$$

where  $k$  is the spring constant of the fold between two adjacent plaquettes, and  $k_p$  is the spring constant of the additional internal fold within a plaquette.

Just as there are optimum design parameters that allow us to extremize the in-plane rigidities, we can also find the optimal design angle pairs that lead to minima of  $B_x$ , by setting  $\partial_\theta B_x|_\alpha = 0$  and  $\partial_\alpha B_x|_\theta = 0$ . This gives us two curves  $\theta_m(\alpha)$  and  $\alpha_m(\theta)$  respectively shown in Fig.3 in the main

text. The green dotted curve  $\theta_m(\alpha)$  starts from  $(\alpha, \theta) \approx (1.1, \pi)$ , and ends at  $(\alpha, \theta) = (\pi/2, \pi)$ . It is asymptotically approximated by  $2.285(\alpha - 1.1) \approx (\pi - \theta_m)^2$  when  $\alpha \rightarrow 1.1$ . The red curve  $\theta_m(\alpha)$  starts from  $(\alpha, \theta) \approx (.913, 0)$ , and ends at  $(\alpha, \theta) = (\pi/2, \pi)$ , and is asymptotically approximated by  $17.752(\alpha_m - 0.913) \approx \theta^2$  when  $\theta \rightarrow 0$ .

Similarly, the bending stiffness per unit width of a single cell in the  $y$  direction is

$$B_y(\alpha, \theta) = kl_e \frac{4\phi_1^2 + 4\frac{k_p}{k} \sin(\frac{\alpha}{2})\phi_2^2 + 2\phi_3^2 + 4\frac{k_p}{k} \sin(\frac{\alpha}{2})\phi_4^2 + 4\phi_5^2}{wl\kappa_y^2} \quad (\text{S.42})$$

### 3.5 Pure bending

Finally, we explain the “pure bending” situation in the main text, borrowing ideas from notions of the pure bending of a beam where curvature is constant. If we demand that a row of unit cells aligned in the  $x$  direction (e.g. the cell  $C_1$  and  $C_2$  in Fig.S.4) undergo exactly the same deformation, this results in  $\phi_2 = \phi_4$ . Furthermore, in this limit, the stretching mode is constrained, so that  $\phi_1 = 0$  for all cells. For this well defined bending deformation, the bending stiffness depends only on the design angles, not on the deformation angles as shown in Eq. (S.41) and Eq. (S.42).

## 4 Numerical simulations of the bending response of a Miura-ori plate

### 4.1 Homogeneous deformation in bent plate is impossible

Here we explain why it is impossible to assemble an entire bent plate by periodically aligning unit cells with identical bending deformation in both the  $x$  and  $y$  direction.

In Fig.S.4, the 4 unit cells  $C_1$ ,  $C_2$ ,  $C_3$  and  $C_4$  have identical bending deformations:  $C_1$  and  $C_2$  align perfectly in the  $x$  direction, which requires that  $\angle O_4O_1O_7 = \angle O_6O_3O_9 = \angle O_{11}O_{13}O_{15}$ .  $C_1$  and  $C_3$ ,  $C_2$  and  $C_4$  align perfectly in the  $y$  direction respectively, which is automatically satisfied by the symmetry of the unit cell. Now the question becomes whether the unit cell  $C_3$  and  $C_4$  can align together? The answer is no. The reasoning is as follows.  $O_3$  and  $O'_3$  are symmetric about plane  $O_6O_{12}O_{13}$ , while  $O_3$  and  $O''_3$  are symmetric about plane  $O_4O_5O_6$ . However plane  $O_6O_{12}O_{13}$  and plane  $O_4O_5O_6$  are not coplanar unless all the deformation angles about the internal folds are zero, which is violated by bending.  $O'_3$  and  $O''_3$  thus do not coincide. In fact  $O'_3 = O''_3$  if and only if  $O_{3y} = O_{5y} = O_{6y}$ , which requires  $\phi_2 = \phi_4 = 0$  from Eq. (S.24), Eq. (S.25), Eq. (S.26) and Eq. (S.28). This is the in-plane stretching mode instead of the bending mode. In conclusion, in the bent Miura-ori plate, the deformation must be inhomogeneous.

### 4.2 Simulation model

In this subsection, we explain the bending model and the strategies used to bend the Miura-ori plate.

We endow these triangulated meshes with elastic stretching and bending modes to capture the in-plane and out-of-plane deformation of thin sheets. The stretching mode simply treats each edge in the mesh as a linear spring, all edges having the same stretching stiffness. Accordingly, the magnitude of the restorative elastic forces applied to each node in a deformed edge with rest length

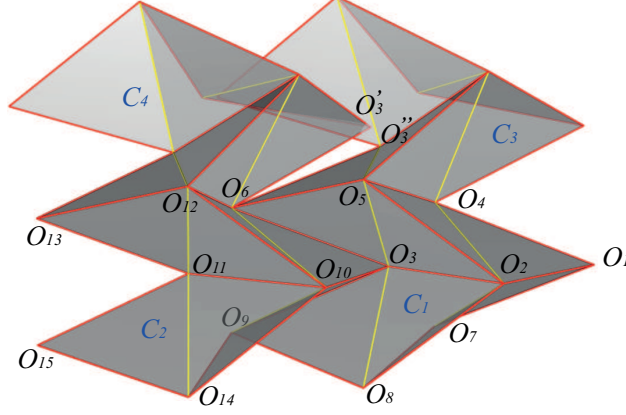


Figure S.4: 4 unit cells with identical bending deformation cannot be aligned together to form an entire plate. See the text for details.

$x_0$  and stretching stiffness  $k$  is given by  $\frac{k_s}{x_0}(x' - x_0)$  and the energy contained in a deformed edge is given by

$$\frac{k_s}{2x_0}(x' - x_0)^2 \quad (\text{S.43})$$

The  $x_0$  term in denominator of the stretching mode ensures mesh-independence. The bending mode is characterized in terms of four vectors  $u_1, u_2, u_3$  and  $u_4$ , each of which is applied to a node in a pair of adjacent triangles. Defining the weighted normal vectors  $N_1 = (x_1 - x_3) \times (x_1 - x_4)$  and  $N_2 = (x_2 - x_4) \times (x_2 - x_3)$  and the shared edge  $E = x_4 - x_3$ , we may write

$$u_1 = |E| \frac{N_1}{|N_1|^2} \quad (\text{S.44})$$

$$u_2 = |E| \frac{N_2}{|N_2|^2} \quad (\text{S.45})$$

$$u_3 = \frac{(x_1 - x_4) \cdot E}{|E|} \frac{N_1}{|N_1|^2} + \frac{(x_2 - x_4) \cdot E}{|E|} \frac{N_2}{|N_2|^2} \quad (\text{S.46})$$

$$u_4 = -\frac{(x_1 - x_3) \cdot E}{|E|} \frac{N_1}{|N_1|^2} - \frac{(x_2 - x_3) \cdot E}{|E|} \frac{N_2}{|N_2|^2}. \quad (\text{S.47})$$

The relative magnitudes of these vectors constitute a pure geometric bending mode for a pair of adjacent triangles. For pairs of adjacent triangles that *do not* straddle the fold line, the force on each vertex is given by

$$F_i = k_b \left( \frac{\theta}{2} - \frac{\theta_0}{2} \right) u_i \quad (\text{S.48})$$

where  $k_b$  is the bending stiffness and  $\theta$  is the angle between  $N_1$  and  $N_2$  that makes each  $u_i$  a restorative force. For pairs of adjacent triangles that straddle folds,  $\theta_0$  is non-zero and shifts the rest angle of the adjacency to a non-planar configuration. The bending energy contained in a pair of adjacent triangles is given by

$$E_b = k_b \int_{\theta_0}^{\theta} \left( \frac{\theta}{2} - \frac{\theta_0}{2} \right) d\theta \quad (\text{S.49})$$



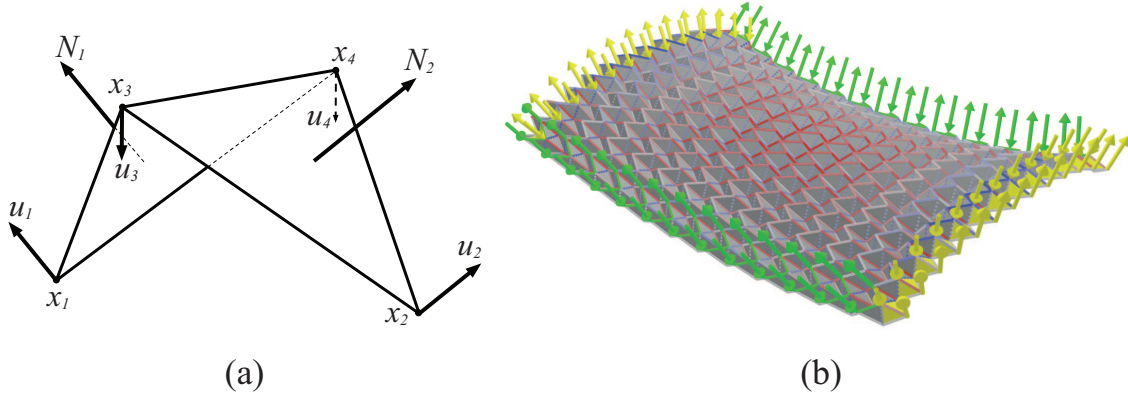


Figure S.5: Simulation model. (a) A single bending adjacency. The vectors  $u_i$  illustrate the purely geometric bending mode and  $N_1$  and  $N_2$  are the weighted normals of the adjacent triangles. (b) The left-right bending strategy is shown in yellow and the up-down bending strategy is shown in green. Each arrow represents a force applied to its incident vertex. Left-right force directions bisect the yellow adjacencies and are perpendicular to the shared edge and up-down force directions are normal to the plane spanned by each pair of green edges.

with a precise form of

$$E_b = k_b \left( \frac{\theta}{2} - \frac{\theta_0}{2} \right)^2 \quad (\text{S.50})$$

which is quadratic in  $\theta$  for  $\theta \sim \theta_0$ .

We introduce viscous damping so that the simulation eventually comes to rest. Damping forces are computed at every vertex with different coefficients for each oscillatory mode, bending and stretching. We distinguish between these two modes by projecting the velocities of the vertices in an adjacency onto the bending mode, and the velocities of the vertices in an edge onto the stretching mode.

We use the Velocity Verlet numerical integration method to update the positions and velocities of the vertices based on the forces from the bending and stretching model and the external forces from our bending strategies. At any time  $t + \Delta t$  during the simulation we can approximate the position  $x(t + \Delta t)$  and the velocity  $\dot{x}(t + \Delta t)$  of a vertex as

$$x(t + \Delta t) = x(t) + \dot{x}(t) \Delta t + \frac{1}{2} \ddot{x}(t) \Delta t^2 \quad (\text{S.51})$$

$$\dot{x}(t + \Delta t) = \dot{x}(t) + \frac{\ddot{x}(t) + \ddot{x}(t + \Delta t)}{2} \Delta t \quad (\text{S.52})$$

A single position, velocity and acceleration update follows a simple algorithm.

- Compute  $x(t + \Delta t)$
- Compute  $\ddot{x}(t + \Delta t)$  using  $x(t + \Delta t)$  for stretching and bending forces and  $\dot{x}(t)$  for damping forces
- Compute  $\dot{x}(t + \Delta t)$

Figure S.6: 3D geometry of a bent Miura plate made of 21 by 21 unit cells with  $\alpha = \theta = \pi/3$ . For better display purpose, we use an example with pronounced deformation. However in the simulation we have done, we make sure that the radius of curvature is at least 10 times larger than the plate size, such that the deformation is within linear regime. Readers may want to play with different toolbar options to better visualize the geometry.

Note that this algorithm staggers the effects of damping on the simulation by  $\Delta t$ .

In simulation, the Miura-ori plate is made of 21 by 21 unit cells, 21 being the number of unit cells in one direction.  $\alpha$  varies from  $20^\circ$  to  $70^\circ$ , and  $\theta$  varies from  $30^\circ$  to  $150^\circ$ , both every  $10^\circ$ . We design two bending strategies, each of which corresponds to a pair of opposite boundaries. The left-right bending strategy identifies the adjacencies with  $O_2O_3$  shared edges on left boundary unit cells and  $O_1O_2$  shared edges on right boundary unit cells (highlighted in yellow in Fig.S.5b). For each of these adjacencies we apply equal and opposite forces to the vertices on their shared edge, the directions of which are determined to lie in the bisecting plane of  $O_1O_2O_4$  and  $O_1O_2O_7$  (left boundary unit cells) and  $O_2O_3O_5$  and  $O_2O_3O_8$  (right boundary unit cells) and perpendicular to the shared edge. The up-down bending strategy identifies the top edges of each unit cell on the up and down boundaries of the pattern (shown in green in Fig.S.5b). Each unit cell has one such pair of edges and we apply equal and opposite forces to the not-shared vertices in this pair, the directions of which are normal to the plane spanned by the pair of edges. We take out the 11th row and 11th column of vertices on the top surface as two sets of points to locally interpolate the curvature near the center of the plate in  $x$  and  $y$  direction respectively. The largest difference of  $\nu_b$  for the same design angle pairs  $\alpha$  and  $\theta$  between both B.Cs applied is less than 0.5%.

By applying the bending strategies described above, we are able to generate deformed Miura-ori plates in simulation. See the simulation result in the below interactive Fig.S.6 to understand the saddle geometry that results from bending the Miura-ori. Readers may want to play with different toolbar options to better visualize the geometry.

## References

- [1] A.E. Lobkovsky, Boundary layer analysis of the ridge singularity in a thin plate, *Phys. Rev. E* **53** (1996), pp.3750. (doi:10.1103/PhysRevE.53.3750)
- [2] R. Bridson, S. Marino, and R. Fedkiw, Simulation of Clothing with Folds and Wrinkles. *ACM SIGGRAPH/Eurographics Symposium on Computer Animation (SCA)* (2003), pp.28-36.